JOURNAL OF COMPUTATIONAL PHYSICS **131,** 267–279 (1997)
ARTICLE NO. CP965572

A High-Order Accurate Discontinuous Finite Element Method for the Numerical Solution of the Compressible Navier–Stokes Equations

F. Bassi* and S. Rebay†

*Dipartimento di Energetica, Università degli Studi di Ancona, Via Brecce Bianche, 60131 Ancona, Italy; †Dipartimento di Ingegneria Meccanica, Università degli Studi di Brescia, Via Branze 38, 25121 Brescia, Italy
E-mail: rebay@bsing.ing.unibs.it

Received January 17, 1996; revised July 29, 1996

This paper deals with a high-order accurate discontinuous finite element method for the numerical solution of the compressible Navier–Stokes equations. We extend a discontinuous finite element discretization originally considered for hyperbolic systems such as the Euler equations to the case of the Navier–Stokes equations by treating the viscous terms with a mixed formulation. The method combines two key ideas which are at the basis of the finite volume and of the finite element method, the physics of wave propagation being accounted for by means of Riemann problems and accuracy being obtained by means of high-order polynomial approximations within elements. As a consequence the method is ideally suited to compute high-order accurate solution of the Navier–Stokes equations on unstructured grids. The performance of the proposed method is illustrated by computing the compressible viscous flow on a flat plate and around a NACA0012 airfoil for several flow regimes using constant, linear, quadratic, and cubic elements.

1. INTRODUCTION

The discontinuous Galerkin method was introduced by Reed and Hill [23] and successively analyzed by Lesaint and Raviart [17, 18] for the linear advection equation. More recently, Cockburn and Shu [9, 10, 12], and Cockburn, Hou, and Shu [11] devised a high order accurate (both in space and time) total variation bounded (TVB) ''Runge–Kutta discontinuous Galerkin'' (RKDG) method for the solution of nonlinear systems of conservation laws. The TVB property of the RKDG method is enforced by means of a ''slope limiting'' procedure designed to control the deviation from the element mean of the numerical solution. Extensions of the RKDG method to systems of equations involving second-order and third-order operators have been recently proposed by Cockburn *et al.* [13, 14].

In this work we extend a high-order discontinuous finite element method for the numerical solution of the Euler equations, which has proven to be very effective in several test cases [2–4], to the case of the compressible Navier–Stokes equations. The space discretization of the inviscid terms of the Navier–Stokes equations is constructed following the ideas described in the works of Cockburn *et al.*, except for the limiting procedure. As shown, for example, in [6], no limiting is in fact needed even for inviscid flows, provided that the solution is sufficiently smooth. The space discretization of the viscous terms is constructed by resorting to a mixed finite element formulation. However, instead of using the Raviart–Thomas formulation as in [13, 14], we approximate both the unknown and its gradient in the same discontinuous function space (see Section 2).

The method combines different features commonly associated to finite element and to finite volume methods. As in classical finite element methods, in fact, accuracy is obtained by means of high-order polynomial approximation within an element rather than by wide stencils as in the case of finite volume schemes. The physics of wave propagation is, however, accounted for by solving the (approximate) Riemann problems that arise from the discontinuous representation of the solution at element interfaces. In this respect the method is therefore similar to a finite volume scheme.

The discontinuous finite element method is more suitable than common finite volume methods to compute high-order accurate solutions on unstructured grids. In fact, high-order accurate finite volume methods are constructed by employing wider stencils to compute fluxes across cell interfaces. In practice, due to the presence of points aligned along grid directions, this approach is straightforward only when using structured grids. Recently some successful high-order accurate finite volume schemes for unstructured meshes have nevertheless been developed (see, for example, Barth [1], Harten and Chakravarthy [15]). Unfortunately, high-order finite volume methods for unstructured grids are rather complex algorithms. On the contrary, high-order accurate discontinuous finite element method discretizations are constructed by means

0021-9991/97 $25.00

of high order polynomials within elements, which poses no problems with structured as well as with unstructured grids.

The outline of the present work is as follows. In Section 2 we describe the discontinuous Galerkin formulation for the Navier–Stokes equations. For completeness, we briefly describe the method also for the inviscid terms of the equations, even if their treatment follows closely that introduced by Cockburn and Shu. More details can be found in [9–12]. The performance of the method is illustrated in Section 3 by computing the laminar viscous compressible flow on a flat plate at M = 0.3 and Re = 10^6 and the flow around a NACA0012 airfoil in the three different conditions considered in the GAMM workshop [21]; i.e., the subsonic case at an angle of attack $\alpha = 10°$, Mach number M = 0.8, and Reynolds number Re = 73; the supersonic case at $\alpha = 10°$, M = 2, Re = 106; and the more difficult subsonic case at $\alpha = 0°$, M = 0.5, and Re = 5000. Numerical solutions using constant, linear, quadratic, and cubic elements are provided. Section 4 is devoted to the conclusions.

2. DISCONTINUOUS GALERKIN FORMULATION

We consider the two-dimensional Navier–Stokes equations written in conservation form

$$\partial_t \mathbf{u} + \nabla \cdot \mathbf{F}_e(\mathbf{u}) - \nabla \cdot \mathbf{F}_v(\mathbf{u}, \nabla \mathbf{u}) = 0, \tag{1}$$

equipped with suitable initial-boundary conditions. The conservative variables $\mathbf{u}$ and the cartesian components $\mathbf{f}_e(\mathbf{u})$ and $\mathbf{g}_e(\mathbf{u})$ of the inviscid (Euler) flux function $\mathbf{F}_e(\mathbf{u})$ are given by

$$\mathbf{u} = \begin{Bmatrix} \rho \\ \rho u \\ \rho v \\ \rho e \end{Bmatrix}, \quad \mathbf{f}_e(\mathbf{u}) = \begin{Bmatrix} \rho u \\ \rho uu + p \\ \rho vu \\ \rho hu \end{Bmatrix}, \quad \mathbf{g}_e(\mathbf{u}) = \begin{Bmatrix} \rho v \\ \rho uv \\ \rho vv + p \\ \rho hv \end{Bmatrix}, \tag{2}$$

where ρ is the fluid density, u and v are the velocity components, p is the pressure, and e is the total internal energy per unit mass. The total enthalpy per unit mass h is defined as $h = e + p/\rho$. By assuming that the fluid obeys to the perfect gas state equation, p can be computed as $p = (\gamma - 1)\rho[e - (u^2 + v^2)/2]$, where γ indicates the ratio between the specific heats of the fluid.

The cartesian components $\mathbf{f}_v(\mathbf{u}, \nabla \mathbf{u})$ and $\mathbf{g}_v(\mathbf{u}, \nabla \mathbf{u})$ of the viscous flux function $\mathbf{F}_v(\mathbf{u}, \nabla \mathbf{u})$ are given by

$$\mathbf{f}_v(\mathbf{u}, \nabla \mathbf{u}) = \mu \begin{Bmatrix} 0 \\ 2u_x + \lambda(u_x + v_y) \\ v_x + u_y \\ u[2u_x + \lambda(u_x + v_y)] + v(v_x + u_y) + \gamma/Pr\, e_x \end{Bmatrix}, \tag{3}$$

$$\mathbf{g}_v(\mathbf{u}, \nabla \mathbf{u}) = \mu \begin{Bmatrix} 0 \\ v_x + u_y \\ 2v_x + \lambda(u_x + v_y) \\ u(v_x + u_y) + v[2v_y + \lambda(u_x + v_y)] + \gamma/Pr\, e_y \end{Bmatrix}, \tag{4}$$

where μ is the dynamic viscosity coefficient, Pr is the Prandtl number, and, using the Stokes hypothesis, $\lambda = -\frac{2}{3}$. The derivatives of the primitive variables such as u_x, u_y, ... can be easily computed by expanding the derivatives of the conservative variables. For example, $(\rho u)_x = \rho_x u + \rho\, u_x$, and, therefore, $u_x = (1/\rho)[(\rho u)_x - \rho_x u]$.

By multiplying by a "test function" $\mathbf{v}$ and integrating over the domain Ω we obtain the weighted residual formulation,

$$\begin{aligned} &\int_\Omega \mathbf{v}\partial_t \mathbf{u}\, d\Omega + \int_\Omega \mathbf{v}\nabla \cdot \mathbf{F}(\mathbf{u}, \nabla \mathbf{u})\, d\Omega \\ &\quad = \sum_E \left[\int_E \mathbf{v}\partial_t \mathbf{u}\, d\Omega + \int_E \mathbf{v}\nabla \cdot \mathbf{F}(\mathbf{u}, \nabla \mathbf{u})\, d\Omega \right] \\ &\quad = 0 \quad \forall \mathbf{v}, \end{aligned} \tag{5}$$

where $\mathbf{F}(\mathbf{u}, \nabla \mathbf{u}) = \mathbf{F}_e(\mathbf{u}) - \mathbf{F}_v(\mathbf{u}, \nabla \mathbf{u})$, and the integrals over the domain Ω have been expanded into the sum of integrals over a collection of nonoverlapping elements $\{E\}$, which have been assumed to be triangles. By integrating by parts each elemental contribution of eq. (5) which contains the divergence of the Navier–Stokes flux function, we obtain the weak formulation

$$\begin{aligned} \sum_E \Bigg[&\int_E \mathbf{v}\partial_t \mathbf{u}\, d\Omega + \oint_{\partial E} \mathbf{v}\mathbf{F}(\mathbf{u}, \nabla \mathbf{u}) \cdot \mathbf{n}\, d\sigma \\ &- \int_E \nabla \mathbf{v} \cdot \mathbf{F}(\mathbf{u}, \nabla \mathbf{u})\, d\Omega \Bigg] = 0 \quad \forall \mathbf{v}, \end{aligned} \tag{6}$$

where ∂E denotes the boundary of element E.

A discrete analogue of Eq. (6) is obtained by considering, within each element, only the functions $\mathbf{u}_h$ and $\mathbf{v}_h$ given by

$$\mathbf{u}(\mathbf{x}, t)_{h|E} = \sum_{i=1}^{n} \mathbf{U}_i(t)\phi_i^k(\mathbf{x}),$$
$$\mathbf{v}(\mathbf{x})_{h|E} = \sum_{i=1}^{n} \mathbf{V}_i\phi_i^k(\mathbf{x}) \quad \forall \mathbf{x} \in E, \tag{7}$$

where the expansion coefficients $\mathbf{U}_i(t)$ and $\mathbf{V}_i$ denote the degrees of freedom of the numerical solution and of the test function in element E, and the n (shape) functions ϕ_i^k are a base for the polynomial functions P^k. Note that there is no global continuity requirement for $\mathbf{u}_h$ and $\mathbf{v}_h$, which are therefore discontinuous functions across element interfaces. By admitting only the functions $\mathbf{u}_{h|E}$ and $\mathbf{v}_{h|E}$, the summation in Eq. (6) reduces to

$$\frac{d}{dt}\int_E \mathbf{v}_h\mathbf{u}_h\, d\Omega + \oint_{\partial E} \mathbf{v}_h\mathbf{F}(\mathbf{u}_h, \nabla\mathbf{u}_h)\cdot\mathbf{n}\, d\sigma - \int_E \nabla\mathbf{v}_h\cdot\mathbf{F}(\mathbf{u}_h, \nabla\mathbf{u}_h)\, d\Omega = 0 \quad \forall\mathbf{v}_{h|E}. \tag{8}$$

Equation (8) must be satisfied for any element E and for any function $\mathbf{v}_{h|E}$. However, within each element, the $\mathbf{v}_h$ are a linear combination of n shape functions ϕ_i^k, and Eq. (8) is therefore equivalent to the system of n equations,

$$\frac{d}{dt}\int_E \phi_j^k\,\mathbf{u}_h\, d\Omega + \oint_{\partial E} \phi_j^k\mathbf{F}(\mathbf{u}_h, \nabla\mathbf{u}_h)\cdot n\, d\sigma - \int_E \nabla\phi_j^k\cdot\mathbf{F}(\mathbf{u}_h, \nabla\mathbf{u}_h)\, d\Omega = 0, \quad 1 \le j \le n. \tag{9}$$

Notice that, when evaluating the boundary integral of Eq. (9) at an internal interface, the flux terms are not uniquely defined due to the discontinuous function approximation. It is therefore necessary to substitute the Navier–Stokes flux function $\mathbf{F}$ with an interface numerical flux function $\mathbf{H}$ which, in general, depends on both interface states and which introduces a coupling between the unknowns of neighboring elements which would be otherwise completely missing. It is possible to show that Eq. (9) with $\mathbf{F}$ replaced by the numerical flux function $\mathbf{H}$ is nothing but the Galerkin method applied to just one element E with weakly prescribed boundary conditions obtained from the neighboring elements of E if $\partial E \cap \partial\Omega = 0$ or from the boundary conditions of the Navier–Stokes problem if $\partial E \cap \partial\Omega \neq 0$ (for more details see, for the case of the linear advection equation, Section 9.8 of the book by C. Johnson [16]).

We first restrict our attention to the treatment of interface integrals. The inviscid interface integral terms are constructed with a technique traditionally used in upwind finite volume schemes. The flux function $\mathbf{F}_e(\mathbf{u})\cdot\mathbf{n}$ appearing in the second term of Eq. (8) is in fact replaced by a numerical flux function $\mathbf{h}_e(\mathbf{u}^-, \mathbf{u}^+; \mathbf{n})$ which depends on the internal interface state $\mathbf{u}^-$, on the neighboring element interface state $\mathbf{u}^+$, and on the direction of the normal unit vector $\mathbf{n}$. In order to guarantee the formal accuracy of the scheme, the numerical flux is required to satisfy the consistency relations

$$\mathbf{h}_e(\mathbf{u}, \mathbf{u}; \mathbf{n}) = \mathbf{F}(\mathbf{u})\cdot\mathbf{n}, \quad \mathbf{h}_e(\mathbf{u}, \mathbf{v}; \mathbf{n}) = -\mathbf{h}_e(\mathbf{v}, \mathbf{u}; -\mathbf{n}). \tag{10}$$

There are several numerical flux functions satisfying the above criteria such as the Godunov, Lax–Friedrichs, Roe, Engquist–Osher, or HLLE (Harten, Lax, Van Leer, Einfeldt). In this work all the computations have been performed with the "exact" Godunov flux.

The spatial discretization of the viscous term of the Navier–Stokes equations is constructed by resorting to a mixed finite element formulation. The first-order derivatives of the conservative variables appearing in the definitions (3) and (4), in fact, lead to second-order derivatives when we evaluate the divergence of the viscous fluxes. However, second-order derivatives cannot be accommodated directly in a weak variational formulation using a discontinuous function space. We therefore regard the gradient of the conservative variables $\nabla\mathbf{u} = \mathbf{S}(\mathbf{u})$ as auxiliary unknowns of the Navier–Stokes equations, which are therefore reformulated as the following coupled system for the unknowns $\mathbf{S}$ and $\mathbf{u}$,

$$\mathbf{S} - \nabla\mathbf{u} = 0$$
$$\partial_t\mathbf{u} + \nabla\cdot\mathbf{F}_e(\mathbf{u}) + \nabla\cdot\mathbf{F}_v(\mathbf{u}, \mathbf{S}) = 0. \tag{11}$$

System (11) can be approximated by means of a discontinuous finite element formulation in a way similar to that employed for the inviscid part of the equations. The use of an explicit time-stepping scheme greatly simplifies the mixed finite element formulation, since it allows a decoupled solution of system (11). At each time level n, in fact, we first compute a discontinuous approximation of $\mathbf{S}^n$ by solving the first equation of the system and then use $\mathbf{u}^n$ and $\mathbf{S}^n$ to evaluate the inviscid and viscous fluxes of the second equation which is then advanced in time.

The weak formulation of the first equation of system (11) is

$$\int_E \phi_j^k S_h\, d\Omega - \oint_{\partial E} \phi_j^k\mathbf{u}_h\mathbf{n}\, d\sigma + \int_E \nabla\phi_j^k\mathbf{u}_h\, d\Omega = 0, \tag{12}$$

where, due to the discontinuous function approximation at internal interfaces, the unknown $\mathbf{u}_h$ appearing in the

boundary integral is not uniquely defined. In analogy with the procedure described for the inviscid part of the equations, it is therefore necessary to introduce a numerical flux function $\mathbf{H}_s(\mathbf{u}^-, \mathbf{u}^+; \mathbf{n})$ to replace the term $\mathbf{u}_h\mathbf{n}$. Since we are constructing the discrete analogue of a diffusive operator, we define the numerical flux function as the average between the two interface states, i.e., as

$$\mathbf{H}_s(\mathbf{u}^-, \mathbf{u}^+; \mathbf{n}) = \tfrac{1}{2}(\mathbf{u}^- + \mathbf{u}^+)\mathbf{n}. \tag{13}$$

By assembling all Eqs. (12), we obtain a system of equations which, thanks to the block diagonal structure of the mass matrix, can be cheaply solved. The computed auxiliary variables $\mathbf{S}_h$ are then used in the weak form of the second equation of system (11),

$$\begin{aligned}\frac{d}{dt}\int_E \mathbf{v}_h\mathbf{u}_h\,d\Omega + \oint_{\partial E} \phi_j^k\mathbf{F}_e(\mathbf{u}_h)\cdot\mathbf{n}\,d\sigma - \int_E \nabla\phi_j^k\cdot\mathbf{F}_e(\mathbf{u}_h)\,d\Omega \\ + \oint_{\partial E} \phi_j^k\mathbf{F}_v(\mathbf{u}_h, \mathbf{S}_h)\cdot\mathbf{n}\,d\sigma \\ - \int_E \nabla\phi_j^k\cdot\mathbf{F}_v(\mathbf{u}_h, \mathbf{S}_h)\,d\Omega,\end{aligned} \tag{14}$$

in which, once again, the boundary integral contains flux terms which are not uniquely defined. It is therefore necessary to replace the term $\mathbf{F}_v(\mathbf{u}_h, \mathbf{S}_h)\cdot\mathbf{n}$ with the numerical flux function $\mathbf{h}_v(\mathbf{u}^-, \mathbf{S}^-, \mathbf{u}^+, \mathbf{S}^+; \mathbf{n})$, defined in a "centered" way as

$$\mathbf{h}_v(\mathbf{u}^-, \mathbf{S}^-, \mathbf{u}^+, \mathbf{S}^+; \mathbf{n}) = \tfrac{1}{2}[(\mathbf{F}_v(\mathbf{u}^-, \mathbf{S}^-) + \mathbf{F}_v(\mathbf{u}^+, \mathbf{S}^+)]\cdot\mathbf{n}. \tag{15}$$

We now describe the treatment of the boundary integrals when ∂E is part of σ_h. In this case the boundary fluxes must be chosen in order to weakly prescribe the boundary conditions of the problem and will be denoted by $\mathbf{h}_e^*(\mathbf{u}_{bc})$, $\mathbf{H}_s^*(\mathbf{u}_{bc})$, and $\mathbf{h}_v^*(\mathbf{u}_{bc}, \mathbf{S}_{bc})$, where $\mathbf{u}_{bc}$ and $\mathbf{S}_{bc}$ are the boundary conditions of the problem and $\mathbf{h}_e^*$, $\mathbf{H}_s^*$, and $\mathbf{h}_v^*$ are the boundary fluxes for the inviscid contribution to the Navier–Stokes equations and for Eqs. (12) and (14), respectively.

At solid walls $\mathbf{h}_e^*$ is equal to the pressure contribution of the inviscid flux function in the direction normal to the wall, the pressure being taken from the internal boundary state. At inflow/outflow boundaries, $\mathbf{h}_e^*$ is the numerical flux function $\mathbf{h}_e(\mathbf{u}^-, \mathbf{u}_{bc}; \mathbf{n})$, where $\mathbf{u}^-$ is the internal boundary state at the current time level, and $\mathbf{u}_{bc}$ is computed by imposing the available data and the Riemann invariant associated to outgoing characteristics. The same value of $\mathbf{u}_{bc}$ used for $\mathbf{h}_e^*$ is also used to define $\mathbf{H}_s^* = \mathbf{u}_{bc}\mathbf{n}$.

The viscous boundary flux at solid walls is computed as $\mathbf{h}_v^* = \mathbf{F}_v(\mathbf{u}_{bc}, \mathbf{S}_{bc})\cdot\mathbf{n}$, where $\mathbf{u}_{bc}$ is that used for $\mathbf{h}_e^*$. If there are no boundary conditions on $\nabla\mathbf{u}\cdot\mathbf{n}$, we set $\mathbf{S}_{bc} = \mathbf{S}^-$. When such conditions are instead prescribed, the value of $\mathbf{S}_{bc}$ is modified accordingly. For example, at an adiabatic wall boundary $\mathbf{S}_{bc}$ is computed by prescribing the internal gradients of all the primitive variables, except for the gradient of the internal energy, which is modified so as to satisfy the boundary condition $\nabla e\cdot\mathbf{n} = 0$. For inflow/outflow boundaries the viscous boundary flux is instead computed as $\mathbf{h}_v^* = \mathbf{h}_v(\mathbf{u}^-, \mathbf{S}^-, \mathbf{u}_{bc}, \mathbf{S}^-; \mathbf{n})$, where $\mathbf{u}_{bc}$ is that used for $\mathbf{h}_e^*$.

All the integrals appearing in the elemental equations are evaluated by means of Gauss numerical quadrature formulae with a number of integration points consistent with the accuracy required. By assembling together all the elemental contributions the system of ordinary differential equations which govern the evolution in time of the discrete solution can be written as

$$M\frac{dU}{dt} + R(U) = 0, \tag{16}$$

where M denotes the mass matrix, U is the global vector of the degrees of freedom, and $R(U)$ is the residual vector. Due to the block diagonal structure of M, the time integration of this system can be accomplished in a very efficient way by means of an explicit method for initial value problems. In this work we have used a two-stage Runge–Kutta method.

An important issue in mixed finite element formulations is the choice of the approximation space for the auxiliary variables $\mathbf{S}_h$ with respect to the original ones, i.e., the conservative variables $\mathbf{u}_h$. In fact, an inconsistent choice of the two approximation spaces may result in a solution which is polluted by spurious modes. We have not tried to address this issue from a theoretical point of view. In practice we have obtained very good results by using the same type of approximations for both $\mathbf{u}_h$ and $\mathbf{S}_h$. It is important to point out that, even if both $\mathbf{u}_h$ and $\mathbf{S}_h$ have been chosen in the same function space (say that of piecewise discontinuous polynomial P^k of order k inside each element), the auxiliary variable $\mathbf{S}_h$ can, however, be regarded as the sum of an "interface contribution" $\mathbf{S}_h^{(\mathrm{int})} \in P^k$ plus a "volume contribution" $\mathbf{S}_h^{(\mathrm{vol})} \in P^{k-1}$. Since $\mathbf{S}_h^{(\mathrm{int})}$ vanishes when the jump of $\mathbf{u}_h$ at the element interfaces is zero, the auxiliary variable $\mathbf{S}_h \in P^{k-1}$ when the solution $\mathbf{u}_h \in P^k$ is continuous.

In order to define $\mathbf{S}_h^{(\mathrm{int})}$ and $\mathbf{S}_h^{(\mathrm{vol})}$, it is necessary to rewrite the numerical flux function (13) as $\mathbf{u}^- + (\mathbf{u}^+ - \mathbf{u}^-)/2$. By inserting this expression into the boundary integral of Eq. (12), we obtain

$$\begin{aligned}\int_E \phi_j^k\mathbf{S}_h\,d\Omega = \oint_{\partial E} \phi_j^k\mathbf{u}^-\mathbf{n}\,d\sigma + \oint_{\partial E} \phi_j^k\frac{1}{2}(\mathbf{u}^+ - \mathbf{u}^-)\mathbf{n}\,d\sigma \\ - \int_E \nabla\phi_j^k\mathbf{u}_h\,d\Omega.\end{aligned} \tag{17}$$

The first and the last integrals appearing on the right-hand side of Eq. (17) can be (back) integrated by parts so as to obtain a single volume integral, i.e.,

$$\oint_{\partial E} \phi_j^k \mathbf{u}^- \mathbf{n}\, d\sigma - \int_E \nabla \phi_j^k \mathbf{u}_h\, d\Omega = \int_E \phi_j^k \nabla \mathbf{u}_h\, d\Omega.$$

Equation (17) can therefore be rewritten as

$$\int_E \phi_j^k \mathbf{S}_h\, d\Omega = \oint_{\partial E} \phi_j^k \frac{1}{2}(\mathbf{u}^+ - \mathbf{u}^-)\mathbf{n}\, d\sigma + \int_E \nabla \phi_j^k \nabla \mathbf{u}_h\, d\Omega. \tag{18}$$

The contributions $\mathbf{S}_h^{(\mathrm{int})}$ and $\mathbf{S}_h^{(\mathrm{vol})}$ are given by the boundary and by the volume integrals appearing on the right-hand side of Eq. (18), i.e.,

$$\int_E \phi_j^k \mathbf{S}_h^{(\mathrm{int})}\, d\Omega = \oint_{\partial E} \phi_j^k \frac{1}{2}(\mathbf{u}^+ - \mathbf{u}^-)\mathbf{n}\, d\sigma,$$

$$\int_E \phi_j^k \mathbf{S}_h^{(\mathrm{vol})}\, d\Omega = \int_E \phi_j^k \nabla \mathbf{u}_h\, d\Omega.$$

These definitions show that $\mathbf{S}_h^{(\mathrm{int})} \in P^k$, that $\mathbf{S}_h^{(\mathrm{vol})} \in P^{k-1}$, and that the contribution $\mathbf{S}_h^{(\mathrm{int})}$ is proportional to the jump of $\mathbf{u}$ across the element interfaces. As will be shown in the following section, the jump of the computed solution $\mathbf{u}_h$ at element interfaces is indeed very small almost everywhere in the flowfield, where in practice $\mathbf{S} \simeq \mathbf{S}_h^{(\mathrm{vol})} \in P^{k-1}$. However, in those regions where the computed solution displays significant discontinuities, the use of equal interpolation for both primary and auxiliary unknowns seems to provide more accurate results.

3. NUMERICAL EXAMPLES

We present the results obtained in the calculation of the laminar viscous flow on a flat plate and around the NACA0012 airfoil. The first test case is intended to test the method for a high Reynolds number flow in a simple geometry. In the second test, we consider three conditions which, having been considered as validation test cases for shock capturing Navier–Stokes codes in a GAMM workshop, are very well documented in the literature (see, e.g., [19–22]). All the computations have been performed on an HP735/125 workstation using double precision arithmetic.

We first consider the laminar flow on the adiabatic flat plate characterized by a freestream Mach number M = 0.3 and by a Reynolds number based on the freestream condition and on the plate length Re = 10^6. The computations have been performed on a grid consisting of 1600 elements obtained from the triangulation of a structured 51 × 17 "H-grid" with 51 points along the plate and 17 points in the direction normal to the plate. The size of the elements adjacent to the wall in the x and y directions varies from $\Delta x/L = 0.15 \times 10^{-3}$, $\Delta y/L = 0.89 \times 10^{-4}$ at the leading edge to $\Delta x/L = 0.13$, $\Delta y/L = 0.23 \times 10^{-3}$ at the end of the plate. This corresponds to aspect ratios $\Delta x/\Delta y$ of 1.74 and 563, respectively. The value of the nondi-

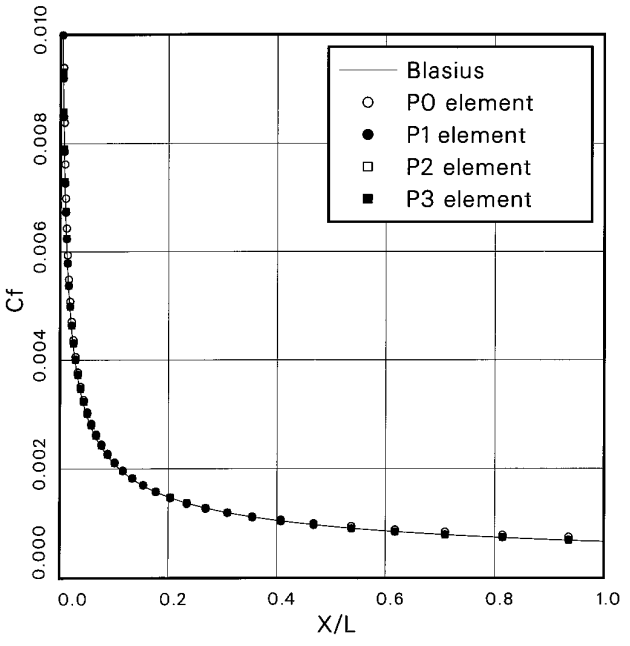

FIG. 1. Skin friction coefficient distribution along the flat plate (Re = 10^6, M = 0.3).

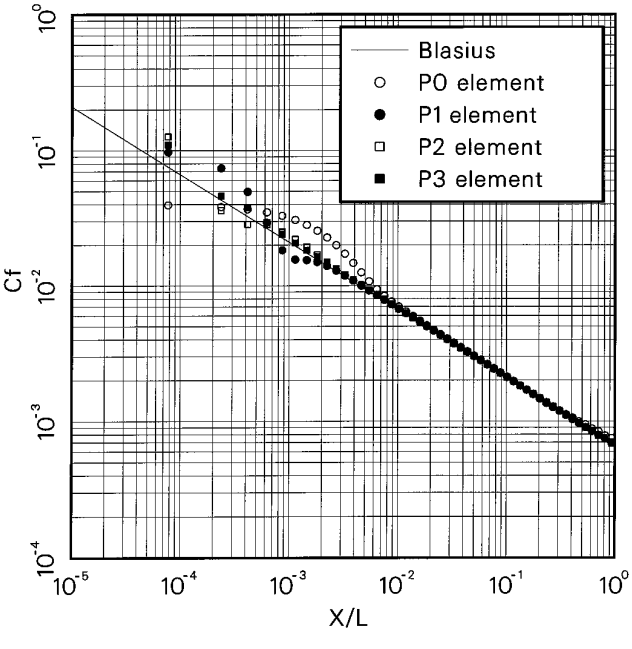

FIG. 2. Logarithmic plot of the skin friction coefficient distribution along the flat plate (Re = 10^6, M = 0.3).

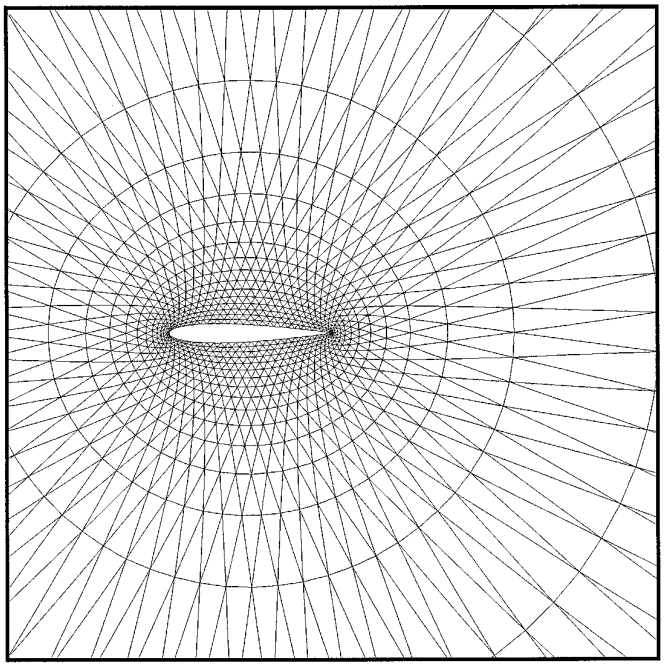

FIG. 3. Grid for the NACA0012 test case (triangulation of a 64 × 16 ''O-grid'').

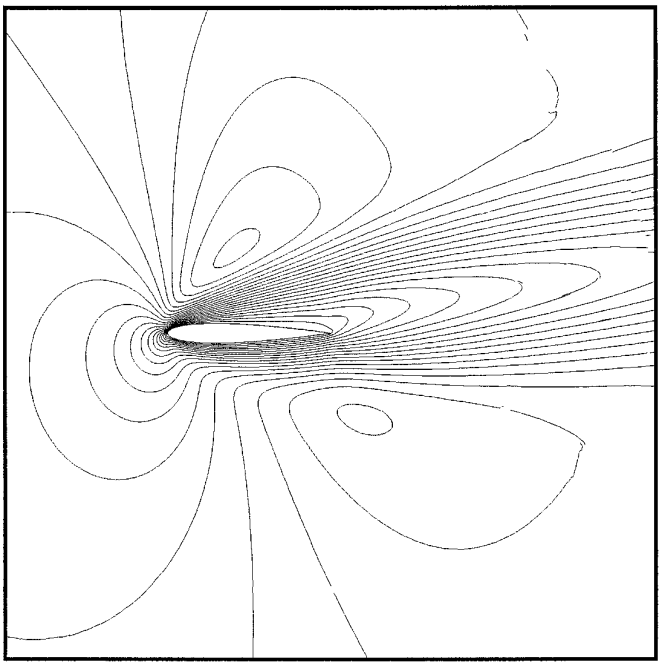

FIG. 5. Quadratic elements; Mach isolines around the NACA0012 airfoil (Re = 73, M = 0.8, $\alpha = 10°$).

mensional distance from the wall to the centroid of the elements adjacent to the wall is of order 1, except for a few elements near the leading edge. We present results obtained with constant, linear, quadratic, and cubic elements, and compare the computed skin friction coefficient with the ''theoretical'' one given by the well-known Blasius formula for the C_f distribution along a flat plate in the case of incompressible flow.

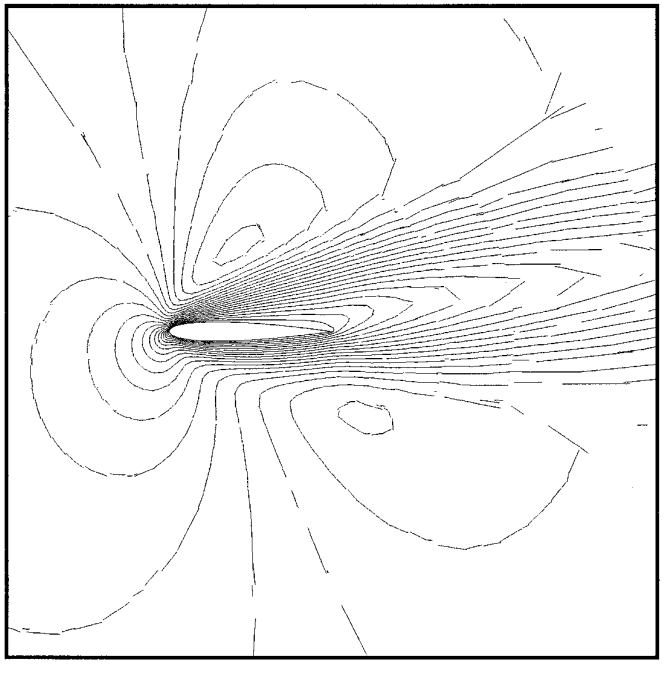

FIG. 4. Linear elements: Mach isolines around the NACA0012 airfoil (Re = 73, M = 0.8, $\alpha = 10°$).

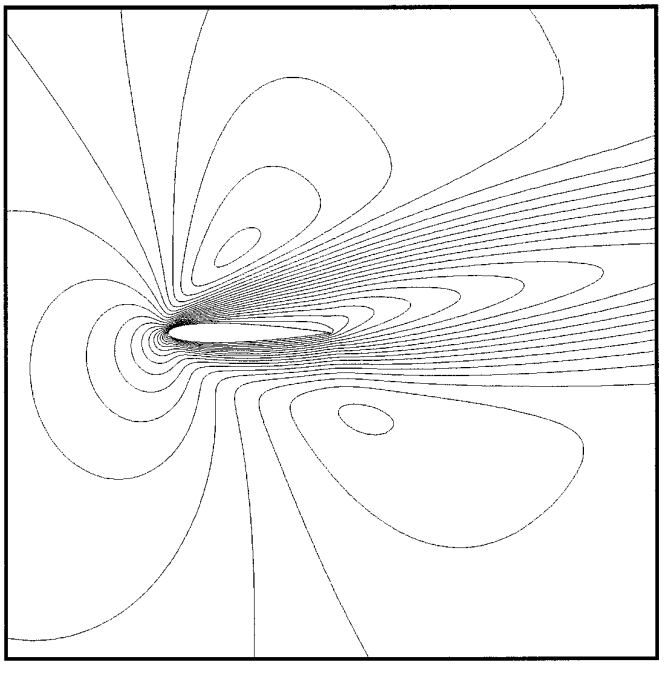

FIG. 6. Cubic elements; Mach isolines around the NACA0012 airfoil (Re = 73, M = 0.8, $\alpha = 10°$).

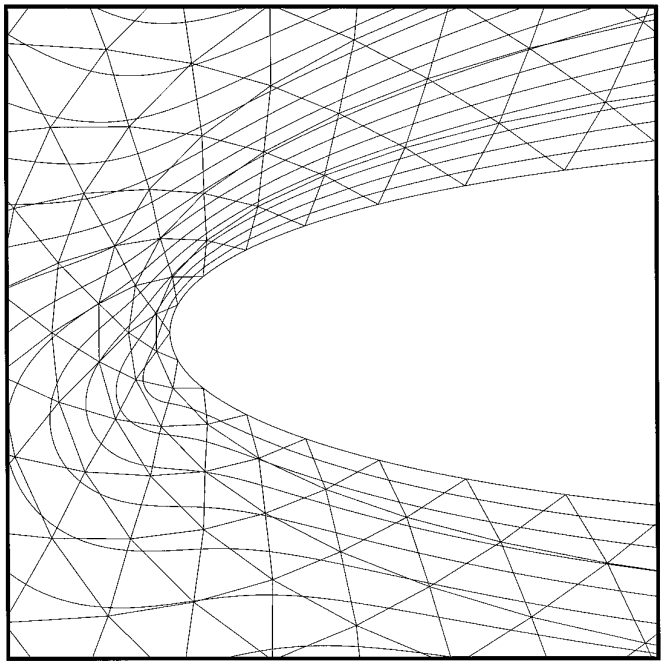

FIG. 7. Cubic elements; detail of the Mach isolines around the leading edge of the NACA0012 airfoil (Re = 73, M = 0.8, $\alpha = 10°$).

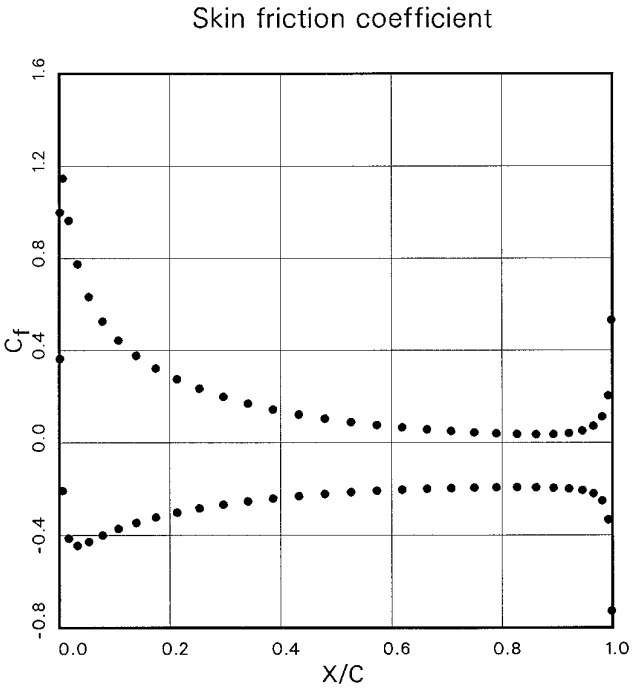

FIG. 9. Cubic elements: skin friction coefficient distribution along the NACA0012 airfoil (Re = 73, M = 0.8, $\alpha = 10°$).

The computed results show very good agreement with the Blasius solution. With reference to Fig. 1, the linear plot of the skin friction coefficient along the plate does not show any significant difference between the various computed solutions and the analytical one. However, the logarithmic plot of Fig. 2 puts in evidence that, in the small region extending up to $x/L = 0.01$ downstream from the leading edge of the plate, high order elements are necessary to obtain an accurate solution.

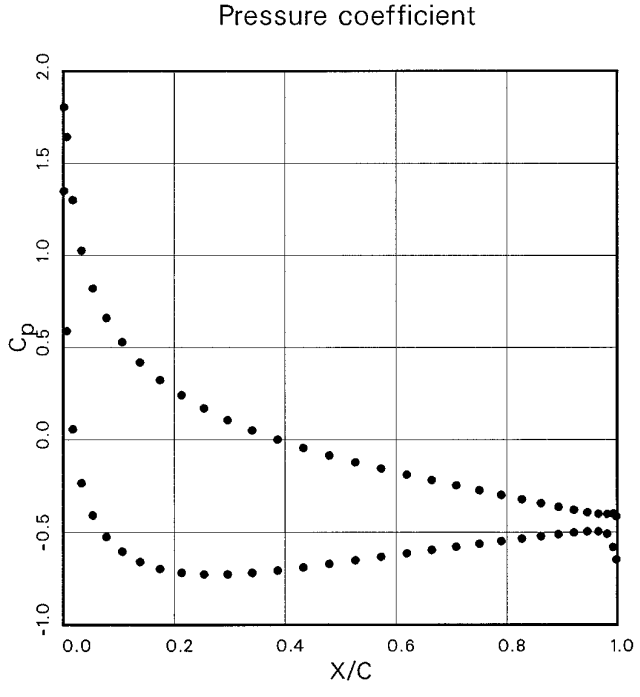

FIG. 8. Cubic elements: pressure coefficient distribution along the NACA0012 airfoil (Re = 73, M = 0.8, $\alpha = 10°$).

We next consider the NACA0012 test case. The computations have been performed on the relatively coarse grid shown in Fig. 3, which is the Delaunay triangulation of a 64 × 16 "O-grid" distribution of points obtained by a conformal mapping method. The larger number refers to the number of elements distributed along the airfoil surface and the smaller one to the number of elements in the radial direction. The grid extends about 20 chords away from the airfoil. The computations have been performed using constant, linear, quadratic, and cubic elements. Note that, in order to put in evidence the discontinuous nature of the numerical solution, all the isolines appearing in the following figures have been plotted without applying any smoothing mechanism.

The first test case is that of the laminar transonic flow at an angle of attack $\alpha = 10°$, freestream Mach number of 0.8, Reynolds number based on the freestream velocity, the airfoil chord equal to 73, and the wall temperature equal to the freestream total temperature. The Mach isolines computed with linear, quadratic, and cubic elements are displayed in Figs. 4, 5, and 6, respectively. (See details in Fig. 7.) As expected, the solution becomes smoother and more accurate by virtue of the increased order of the

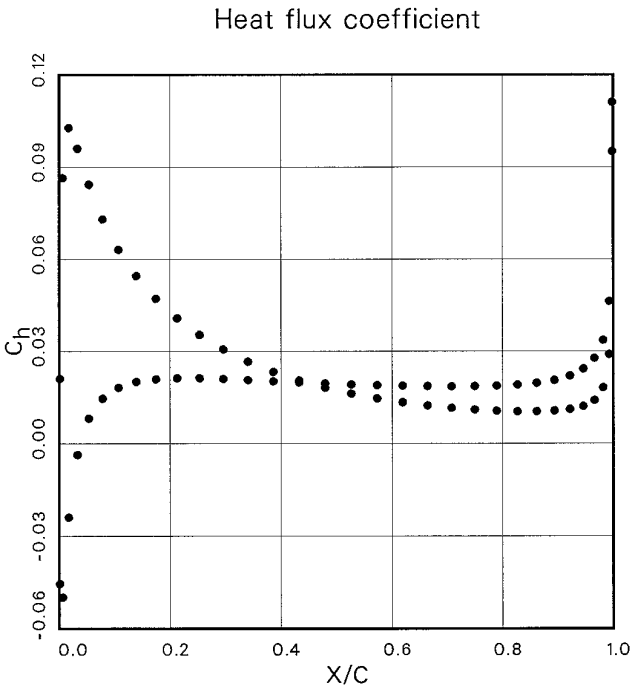

FIG. 10. Cubic elements: heat flux coefficient distribution along the NACA0012 airfoil (Re = 73, M = 0.8, $\alpha = 10°$).

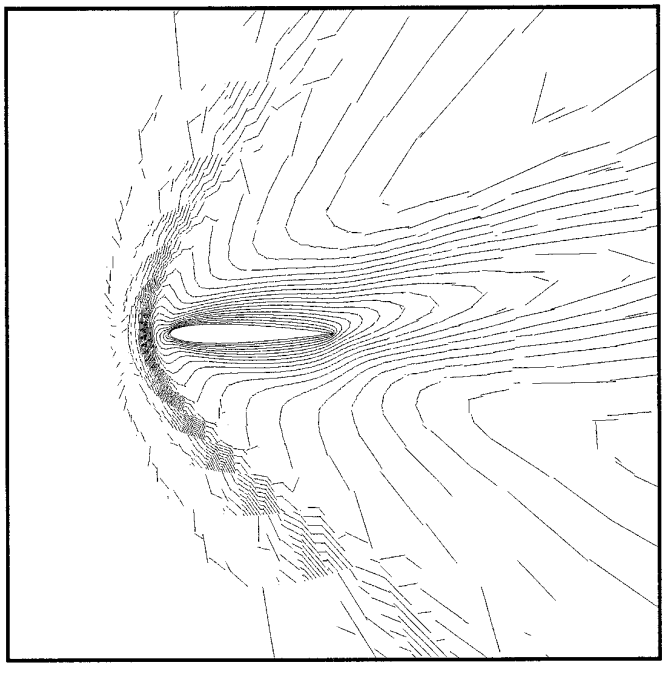

FIG. 11. Linear elements: Mach isolines around the NACA0012 airfoil (Re = 106, M = 2, $\alpha = 10°$).

polynomial approximation when passing from linear to cubic elements. Figures 8, 9, and 10 show the pressure, skin friction, and heat flux coefficient distributions along the airfoil computed with cubic elements. An estimate of the accuracy of the computed solution is given in Table I, which shows the comparison of the lift and drag coefficients obtained with constant, linear, quadratic, and cubic elements, respectively. The values reported seem to indicate that the grid used for this test case is sufficiently fine also for linear elements.

The second test case is that of the laminar supersonic flow at an angle of attack $\alpha = 10°$, freestream Mach number of 2, Reynolds number equal to 106, and wall temperature equal to the freestream total temperature. A distinguishing feature of this test is the presence of a detached bow shock in front of the profile. Figures 11, 12, and 13 show the Mach isolines of the numerical solutions computed by linear, quadratic, and cubic elements, while Figures 14, 15, and 16 show the pressure, skin friction, and heat flux coefficient distributions along the airfoil computed with cubic ele-

TABLE I

Lift (C_l) and Drag (C_d) Coefficients for the NACA0012 Airfoil

Element	Accuracy	C_l	C_d
Constant	1st	0.5844	0.7083
Linear	2nd	0.5360	0.6611
Quadratic	3rd	0.5350	0.6589
Cubic	4th	0.5352	0.6587

Note. Re = 73, M = 0.8, $\alpha = 10°$.

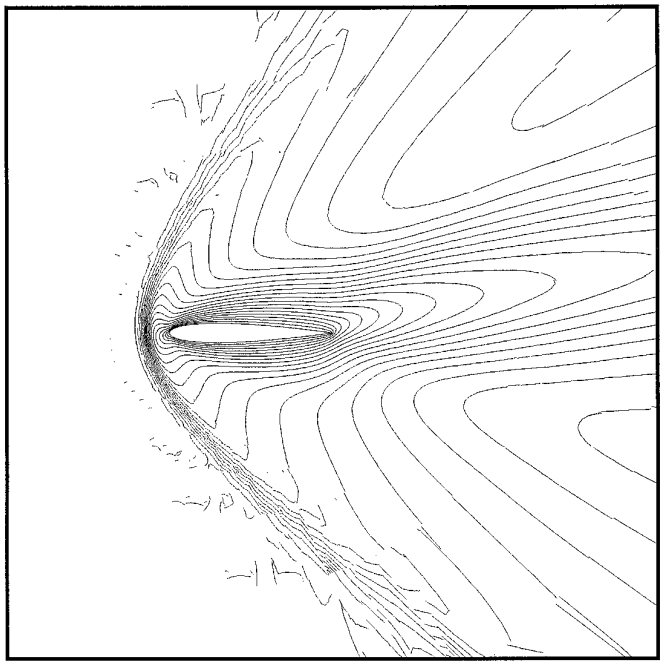

FIG. 12. Quadratic elements; Mach isolines around the NACA0012 airfoil (Re = 106, M = 2, $\alpha = 10°$).

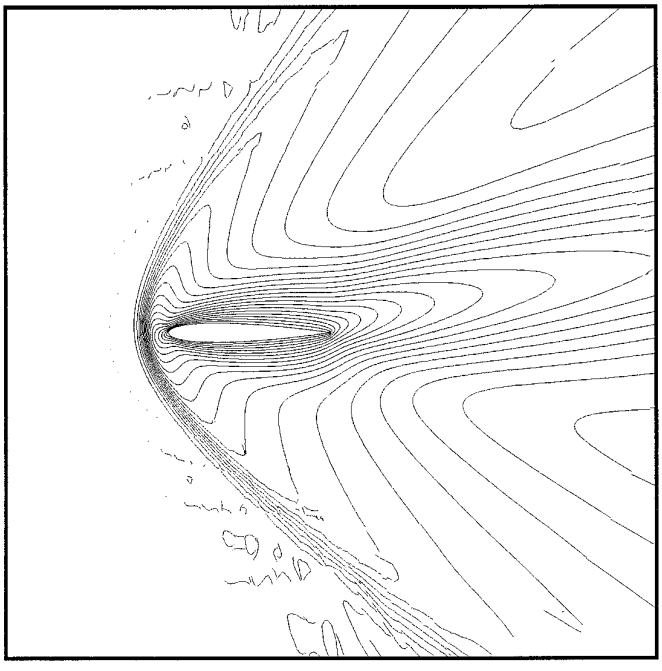

FIG. 13. Cubic elements; Mach isolines around the NACA0012 airfoil (Re = 106, M = 2, α = 10°).

ments. The comments made for the Re = 73 computation apply also for this test case. Note in particular the increasingly better resolution of the bow shock obtained when passing from linear to cubic elements.

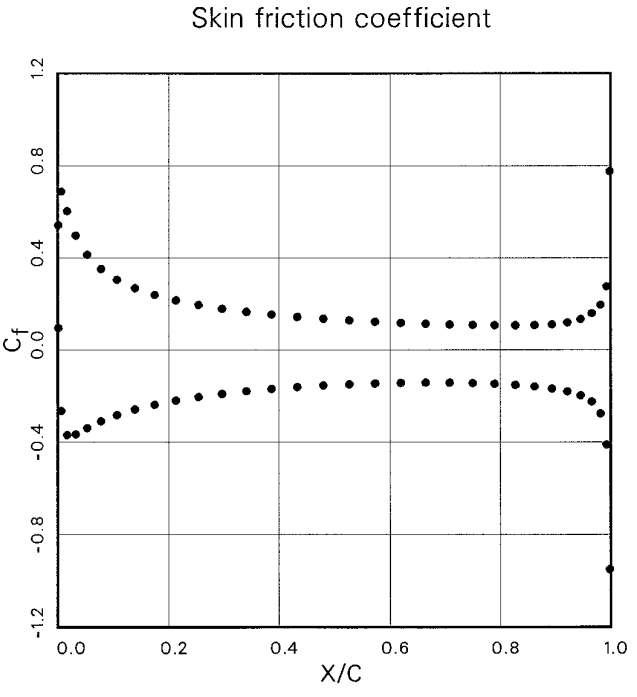

FIG. 15. Cubic elements: skin friction coefficient distribution along the NACA0012 airfoil (Re = 106, M = 2, α = 10°).

A precise quantitative comparison of the results obtained for these two test cases with those published in [21] is difficult because of the large scatter in the results, which seems dependent on both the method and the grid used.

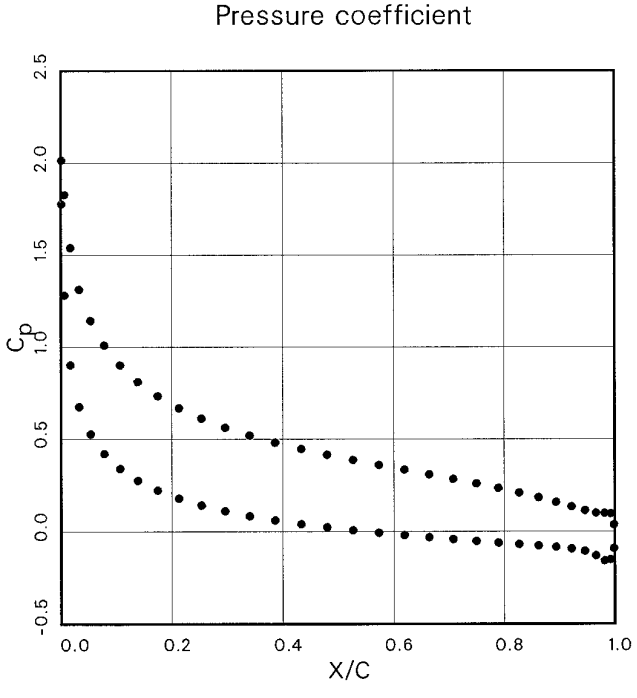

FIG. 14. Cubic elements: pressure coefficient distribution along the NACA0012 airfoil (Re = 106, M = 2, α = 10°).

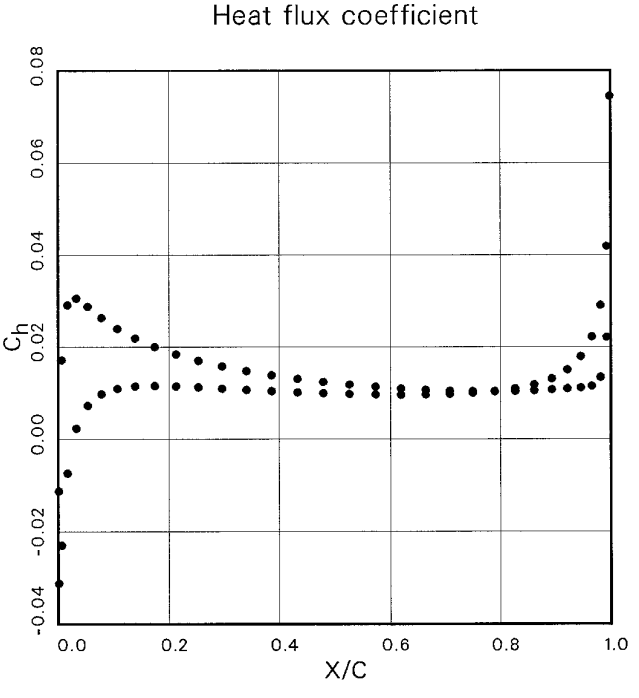

FIG. 16. Cubic elements: heat flux coefficient distribution along the NACA0012 airfoil (Re = 106, M = 2, α = 10°).

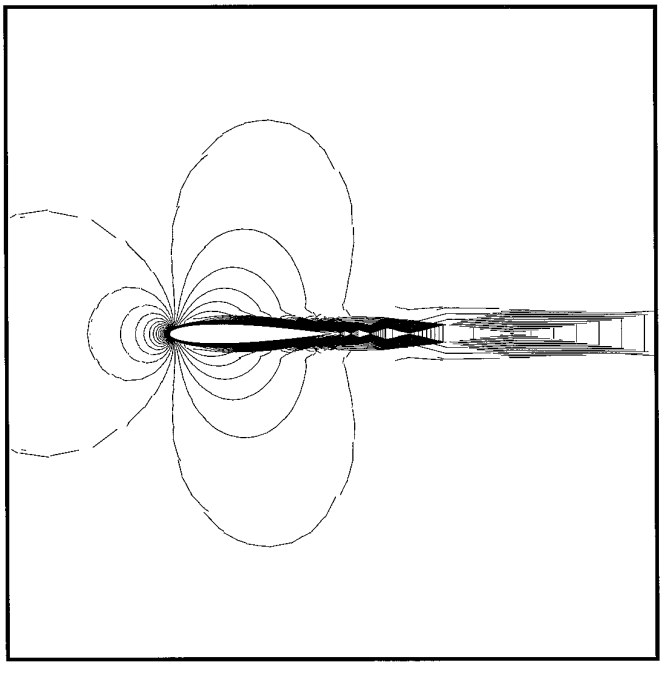

FIG. 17. Linear elements: Mach isolines around the NACA0012 airfoil (Re = 5000, M = 0.5, $\alpha = 0°$).

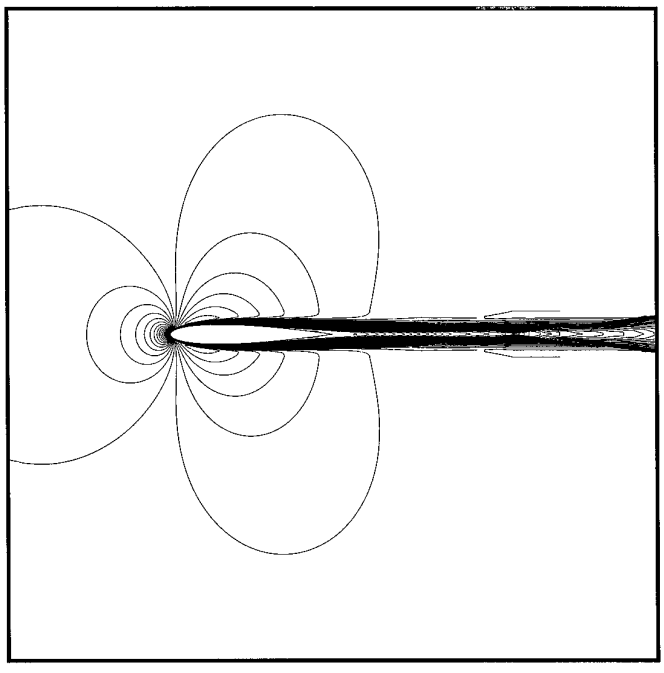

FIG. 19. Cubic elements; Mach isolines around the NACA0012 airfoil (Re = 5000, M = 0.5, $\alpha = 0°$).

However, the coefficient distributions and the lift and drag coefficients shown in the preceding tables compare favorably with the most accurate solution (obtained on very much finer grids) reported in [21]. In particular the peak values of the skin friction and heat flux coefficient distributions are well captured by the present solutions.

The third and more difficult test case is that of the laminar subsonic flow at an angle of attack $\alpha = 0°$, freestream

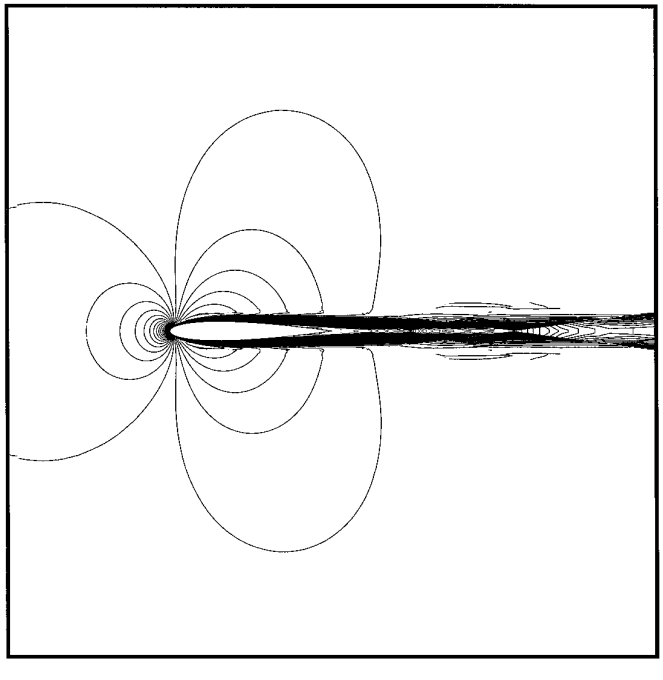

FIG. 18. Quadratic elements: Mach isolines around the NACA0012 airfoil (Re = 5000, M = 0.5, $\alpha = 0°$).

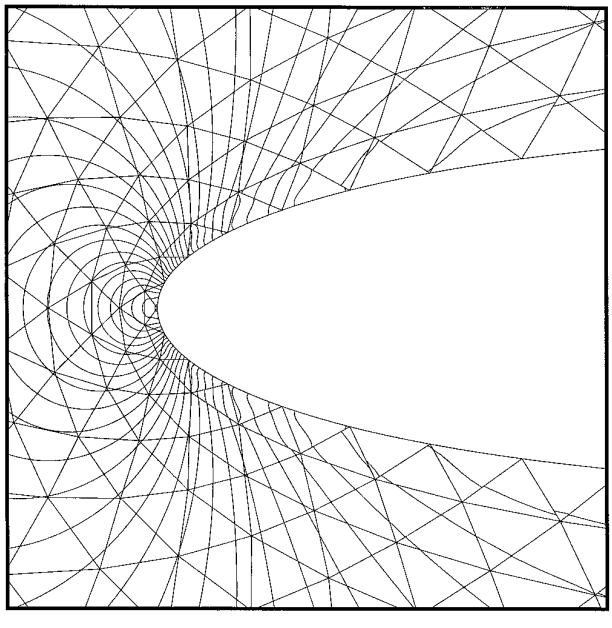

FIG. 20. Cubic elements: detail of the pressure isolines and of the grid around the leading edge of the NACA0012 airfoil (Re = 5000, M = 0.5, $\alpha = 0°$).

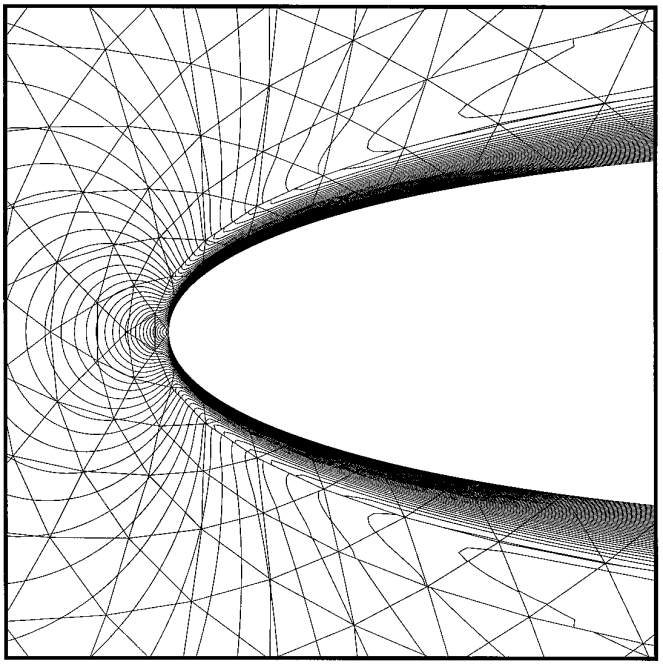

FIG. 21. Cubic elements: detail of the Mach isolines and of the grid around the leading edge of the NACA0012 airfoil (Re = 5000, M = 0.5, $\alpha = 0°$).

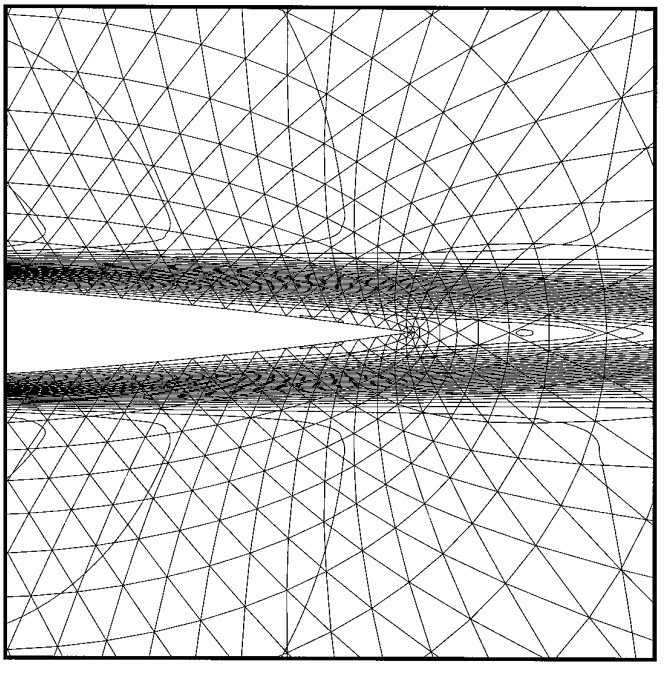

FIG. 22. Cubic elements: detail of the Mach isolines and of the grid around the trailing edge of the NACA0012 airfoil (Re = 5000, M = 0.5, $\alpha = 0°$).

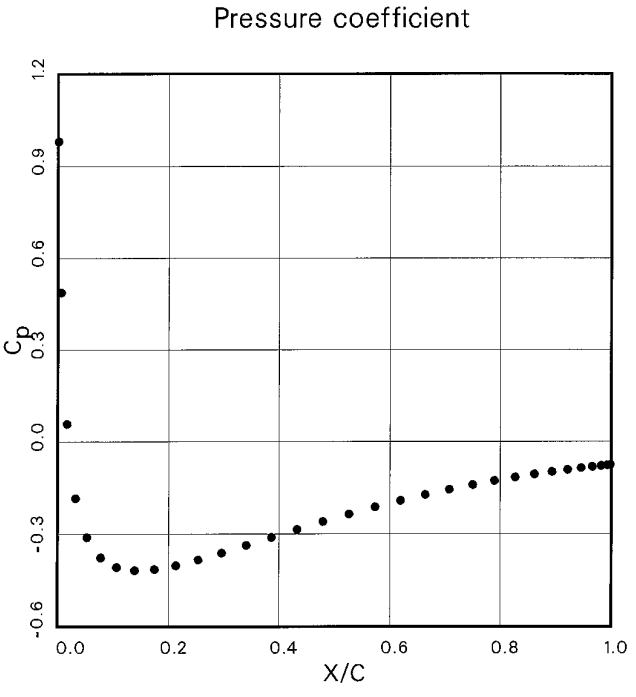

FIG. 23. Cubic elements: pressure coefficient distribution along the NACA0012 airfoil (Re = 5000, M = 0.5, $\alpha = 0°$).

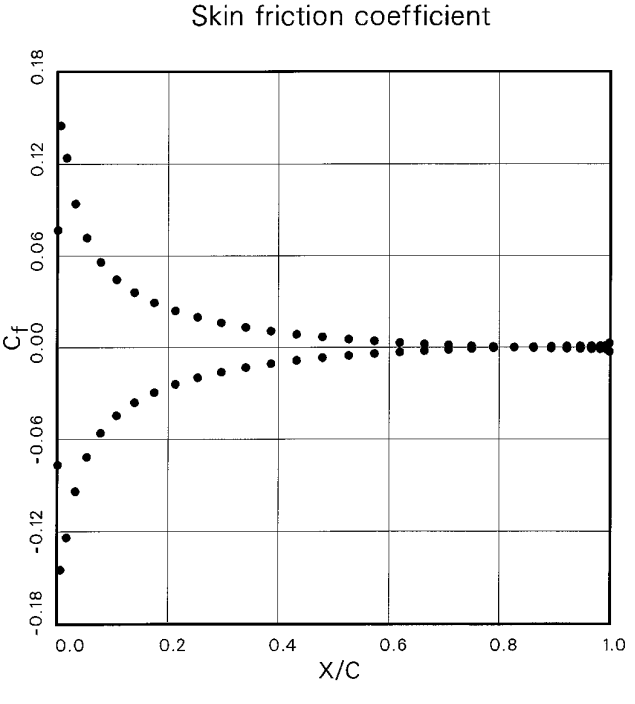

FIG. 24. Cubic elements: skin friction coefficient distribution along the NACA0012 airfoil (Re = 5000, M = 0.5, $\alpha = 0°$).

TABLE II

Pressure Part ($C_{d,p}$) and Viscous Part ($C_{d,v}$) of the Drag Coefficient for the NACA0012 Airfoil

Element	Accuracy	$C_{d,p}$	$C_{d,v}$
Constant	1st	0.03163	0.04942
Linear	2nd	0.01963	0.03051
Quadratic	3rd	0.01991	0.03361
Cubic	4th	0.02208	0.03303

Note. Re = 5000, M = 0.5, $\alpha = 0°$.

Mach number M = 0.5, and Reynolds number equal to 5000. In this case the wall is adiabatic. The Reynolds number is near to the upper limit for steady laminar flow. A distinguishing feature of this test case is the separation of the flow occurring near to the trailing edge which causes the formation of a small recirculation bubble which extends in the near-wake region of the airfoil.

Figures 17, 18, and 19 show the Mach isolines computed by means of linear, quadratic, and cubic elements. The results obtained with cubic elements are further displayed in Figs. 20, 21, and 22, which show details of the flowfield and of the grid around the leading edge and the trailing edge of the airfoil. Figures 23 and 24 show the pressure and skin friction distributions along the airfoil computed with cubic elements, and Table II reports the pressure part and the viscous part of the drag coefficient computed with constant, linear, quadratic, and cubic elements, respectively. The comparison of the values of the drag coefficients computed with cubic elements and those obtained by other authors with both structured and unstructured solvers [19, 20, 22] is given in Table III. This comparison seems to indicate that, on the very coarse grid used, an accurate solution is obtained only with high-order elements. Note in fact that the solution computed with cubic (fourth-order) elements has an accuracy similar to that obtained with common structured and unstructured finite volume schemes on much finer grids.

TABLE III

Comparison of the Pressure Part ($C_{d,p}$) and of the Viscous Part ($C_{d,v}$) of the Drag Coefficient for the NACA0012 Airfoil Computed by the Present Method with Various Structured and Unstructured Solvers

Method	Grid	$C_{d,p}$	$C_{d,v}$
Discontinuous Galerkin with cubic elements	64 × 16	0.02208	0.03303
Triangle scheme from Ref. [20]	320 × 64	0.0229	0.0332
Cell-centered scheme from Ref. [19]	320 × 64	0.0219	0.0337
Cell-vertex scheme from Ref. [22]	256 × 64	0.0227	0.0327
Cell-centered scheme from Ref. [22]	256 × 64	0.02256	0.03301
Cell-centered scheme from Ref. [22]	512 × 128	0.02235	0.03299

Note. Re = 5000, M = 0.5, $\alpha = 0°$.

4. CONCLUSIONS

A high-order accurate discontinuous finite element method for the solution of the compressible Navier–Stokes equations has been presented. The method combines the ability of all finite element methods of constructing in an automatic and reliable way high-order approximations of differential problems on general unstructured meshes with the successful upwind techniques traditionally associated with finite volume schemes and has proven to be very effective in the solution of CFD problems. Our results show that accurate solutions on relatively coarse meshes can be computed, provided that high-order elements are used. General boundary conditions can be accurately and easily prescribed. Finally, the method has proven to be very robust in all the test cases attempted so far.

Work is in progress to implement a two-equation turbulence model and an implicit time integration scheme to improve the efficiency of the method. In the future we also plan to further increase the potentialities of the method by resorting to grid adaption criteria.

REFERENCES

1. T. J. Barth and P. O. Frederickson, AIAA Paper No. 90-0013, 1990 (unpublished).
2. F. Bassi, S. Rebay, and M. Savini, A high resolution discontinuous Galerkin method for hyperbolic problems on unstructured grids, in "Proceedings, IIIrd ICFD, Reading, April 1992," *Numerical Methods in Fluid Dynamics* (Clarendon Press, Oxford, 1993), p. 345.
3. F. Bassi, S. Rebay, and M. Savini, Discontinuous finite element Euler solutions on unstructured adaptive grids, in "Proceedings, IIIrd ICNMFD, Rome, July 6–10, 1992," *Lecture Notes in Physics*, Vol. 414 (Springer-Verlag, New York/Berlin, 1993), p. 245.
4. F. Bassi and S. Rebay. Accurate 2D Euler computations by means of a high order discontinuous finite element method, in "Proceedings, XIVth ICNMFD, Bangalore, July 11–15, 1994," *Lecture Notes in Physics* (Springer-Verlag, New York/Berlin, 1994).
5. F. Bassi and S. Rebay. Discontinuous finite element high order accurate numerical solution of the compressible Navier–Stokes equations, in "Proceedings, IVth ICFD Conference, Oxford, April 3–6, 1995," in *Numerical Methods in Fluid Dynamics*. (Clarendon Press, Oxford, U.K., 1995).
6. F. Bassi and S. Rebay, High-order accurate discontinuous finite element solution of the 2D Euler equations, To appear on *J. Comput. Phys.*
7. K. S. Bey and J. T. Oden, AIAA Paper No. 91-1575-CP, p. 541, 1991 (unpublished).
8. R. Biswas, K. D. Devine, and J. E. Flahertty, Parallel, adaptive finite element methods for conservation laws, *Appl. Numer. Math.* **14,** 255 (1994).
9. B. Cockburn and C.-W. Shu, TVB Runge–Kutta local projection discontinuous Galerkin finite element method for conservation laws II: General framework, *Math. Comput.* **52**, 411 (1989).
10. B. Cockburn and C.-W. Shu, TVB Runge–Kutta local projection

discontinuous Galerkin finite element method for conservation laws III: One dimensional systems, *J. Comput. Phys.* **84**, 90 (1989).

11. B. Cockburn, S. Hou, and C.-W. Shu, The Runge–Kutta local projection discontinuous Galerkin finite element method for conservation laws IV: The multidimensional case, *Math. Comput.* **54,** 545 (1990).
12. B. Cockburn and C.-W. Shu, ''The P^1-RKDG Method for Two-Dimensional Euler Equations of Gas Dynamics,'' ICASE Report No. 91-32, 1991 (unpublished).
13. Z. Chen, B. Cockburn, J. Jerome, and C.-W. Shu, Mixed-RKDG finite element method for the drift-diffusion semiconductor device equation, *VLSI Design* **3**, 145 (1995).
14. Z. Chen, B. Cockburn, C. Gardner, and J. Jerome, Quantum hydrodynamic simulation of hysteresis in the resonant tunneling diode, *J. Comput. Phys.* **117,** 274 (1995).
15. A. Harten and S. R. Chakravarthy, ''Multi-Dimensional ENO Schemes for General Geometries,'' ICASE Report No. 91-76, 1991 (unpublished).
16. C. Johnson, *Numerical Solution of Partial Differential Equations by the Finite Element Method* (Cambridge Univ. Press, Cambridge, UK, 1987).
17. P. Lesaint, *Sur la résolution des systèmes hyperboliques du premier ordre par des méthodes d'elèments finis,* Ph.D. thesis, Université Paris 6, 1975 (unpublished).
18. P. Lesaint and P. A. Raviart, ''On a Finite Element Method to Solve the Neutron Transport Equation,'' in *Mathematical Aspects of Finite Elements in Partial Differential Equations,* edited by C. de Boor (Academic Press, New York, 1974), p. 89.
19. L. Martinelli, ''Calculations of Viscous Flows with a Multigrid Method,'' Ph.D. thesis, Dept. of Mechanical and Aerospace Engineering, Princeton University, 1987.
20. D. J. Mavriplis and A. Jameson, Multigrid solution of the Navier–Stokes equations on triangular meshes, *AIAA J.* **28,** No. 8, 1415 (1990).
21. ''Numerical Simulation of Compressible Navier–Stokes Equations—External 2D Flows Around a NACA0012 Airfoil,'' in GAMM Workshop, December 4–6, 1985, Nice, France (Edt. INRIA, Centre de Rocquefort, de Rennes et de Sophia-Antipolis, 1986).
22. R. Radespiel and R. C. Swanson, ''An Investigation of Cell Centered and Cell Vertex Multigrid schemes for the Navier–Stokes Equations,'' AIAA Paper No. 89-0453, 1989 (unpublished).
23. W. H. Reed and T. R. Hill, ''Triangular Mesh Methods for the Neutron Transport Equation,'' Los Alamos Scientific Laboratory Report LA-UR-73-479, 1973 (unpublished).